RESEARCH ARTICLE

AXL and Error-Prone DNA Replication Confer Drug Resistance and Offer Strategies to Treat EGFR-Mutant Lung Cancer

Ashish Noronha[1], Nishanth Belugali Nataraj[1], Joo Sang Lee[2,3], Benny Zhitomirsky[4], Yaara Oren[5,6], Sara Oster[7], Moshit Lindzen[1], Saptaparna Mukherjee[8], Rainer Will[9], Soma Ghosh[1], Arturo Simoni-Nieves[1], Aakanksha Verma[1], Rishita Chatterjee[1], Simone Borgoni[10], Welles Robinson[2], Sanju Sinha[2], Alexander Brandis[11], D. Lucas Kerr[12], Wei Wu[12], Arunachalam Sekar[1], Suvendu Giri[1], Youngmin Chung[3], Diana Drago-Garcia[1], Brian P. Danysh[4], Mattia Lauriola[13], Michelangelo Fiorentino[13], Andrea Ardizzoni[13,14], Moshe Oren[8], Collin M. Blakely[12,15], Jideofor Ezike[4,16], Stefan Wiemann[10], Laxmi Parida[17], Trever G. Bivona[12,15,18], Rami I. Aqeilan[7], Joan S. Brugge[6], Aviv Regev[19], Gad Getz[4,20], Eytan Ruppin[2], and Yosef Yarden[1]

Illustration by Bianca Dunn

ABSTRACT Anticancer therapies have been limited by the emergence of mutations and other adaptations. In bacteria, antibiotics activate the SOS response, which mobilizes error-prone factors that allow for continuous replication at the cost of mutagenesis. We investigated whether the treatment of lung cancer with EGFR inhibitors (EGFRi) similarly engages hypermutators. In cycling drug-tolerant persister (DTP) cells and in EGFRi-treated patients presenting residual disease, we observed upregulation of GAS6, whereas ablation of GAS6's receptor, AXL, eradicated resistance. Reciprocally, AXL overexpression enhanced DTP survival and accelerated the emergence of T790M, an EGFR mutation typical to resistant cells. Mechanistically, AXL induces low-fidelity DNA polymerases and activates their organizer, RAD18, by promoting neddylation. Metabolomics uncovered another hypermutator, AXL-driven activation of MYC, and increased purine synthesis that is unbalanced by pyrimidines. Aligning anti-AXL combination treatments with the transition from DTPs to resistant cells cured patient-derived xenografts. Hence, similar to bacteria, tumors tolerate therapy by engaging pharmacologically targetable endogenous mutators.

SIGNIFICANCE: EGFR-mutant lung cancers treated with kinase inhibitors often evolve resistance due to secondary mutations. We report that in similarity to the bacterial SOS response stimulated by antibiotics, endogenous mutators are activated in drug-treated cells, and this heralds tolerance. Blocking the process prevented resistance in xenograft models, which offers new treatment strategies.

INTRODUCTION

In 1975, Miroslav Radman reported an inducible bacterial DNA repair/mutagenesis system, the SOS response, which is activated upon sudden increases in DNA damage (1). Later studies established that SOS enhances genetic variation by engaging environmental-sensing pathways (2), which initiate transcriptional programs and mutate the genome, thereby potentiating antibiotic resistance (3). Similar mechanisms of stress-induced mutagenesis (SIM) are shared by eukaryotes, arguing against prevailing assumptions that mutations occur purely stochastically (4). More recently, it was demonstrated that SIM was capable of propelling acquired resistance to targeted therapies (5). Furthermore, the mechanistic target of rapamycin was identified as a stress-sensing rheostat that mediates SIM across multiple cancer types (6).

Targeted treatment of cancer consists primarily of tyrosine kinase inhibitors (TKI) and monoclonal antibodies (mAb), but the emergence of resistance limits the efficacy of both these agents (7). Nevertheless, despite a wide variation in the mechanisms of resistance, many of them coalesce into a few convergences, including *de novo* mutagenesis and bypass routes (8). Although the sequence of events preceding the establishment of resistant clones is poorly understood, one commonality entails a transitory state, called drug-tolerant persister (DTP; ref. 9). To determine the mechanisms driving the transformation of DTP cells to resisters, we studied lung cancer models that express mutant forms of EGFR. Three generations of TKIs have been developed to overcome the deleterious effects of EGFR mutations. The majority of patients initially respond to treatments with erlotinib and other first-generation TKIs, but drug resistance inevitably

[1]Department of Biological Regulation, Weizmann Institute of Science, Rehovot, Israel. [2]Cancer Data Science Lab, NCI, NIH, Bethesda, Maryland. [3]Next-Gen Medicine Lab, School of Medicine and Department of Artificial Intelligence, Sungkyunkwan University, Suwon, Republic of Korea. [4]Broad Institute of MIT and Harvard, Cambridge, Massachusetts. [5]Klarman Cell Observatory, Broad Institute of MIT and Harvard, Cambridge, Massachusetts. [6]Department of Cell Biology, Harvard Medical School, Boston, Massachusetts. [7]Lautenberg Center for Immunology and Cancer Research, Institute for Medical Research Israel-Canada, Hebrew University-Hadassah Medical School, Jerusalem, Israel. [8]Department of Molecular Cell Biology, Weizmann Institute of Science, Rehovot, Israel. [9]Genomics and Proteomics Core Facility, German Cancer Research Center (DKFZ), Heidelberg, Germany. [10]Division of Molecular Genome Analysis, German Cancer Research Center (DKFZ), Heidelberg, Germany. [11]Life Sciences Core Facilities, Weizmann Institute of Science, Rehovot, Israel. [12]Department of Medicine, University of California, San Francisco, California. [13]Department of Experimental, Diagnostic and Specialty Medicine (DIMES), University of Bologna, Bologna, Italy. [14]Medical Oncology IRCCS Azienda Ospedaliero, University of Bologna, Bologna, Italy. [15]Helen Diller Family Comprehensive Cancer Center, University of California, San Francisco, California. [16]Computational and Systems Biology Program, Massachusetts Institute of Technology, Cambridge, Massachusetts. [17]Thomas J. Watson Research Center, IBM Research, Yorktown Heights, New York. [18]Department of Cellular and Molecular Pharmacology, University of California, San Francisco, California. [19]Genentech Inc., South San Francisco, California. [20]Cancer Center and Department of Pathology, Massachusetts General Hospital Cancer Center, Harvard Medical School, Boston, Massachusetts.

Corresponding Author: Yosef Yarden, Department of Biological Regulation, Weizmann Institute of Science, Rehovot 76100, Israel. Phone: 972-8-934-3974; Fax: 972-8-934-2488; E-mail: yosef.yarden@weizmann.ac.il

Cancer Discov 2022;12:2666–83

doi: 10.1158/2159-8290.CD-22-0111

evolves, due mainly to the T790M mutation (10–12), *MET* amplification (13), or stimulation of the transcription-driven epithelial–mesenchymal transition (EMT) program. Second- and third-generation TKIs (e.g., osimertinib) have also been developed, but their application is similarly limited by acquired resistance.

It is conceivable that mechanisms enabling adaptive mutability help hardwire the ability of DTP cells to survive. We assumed that the small group of receptor tyrosine kinases (RTK), which undergo upregulation in response to TKIs (14–18), drives the persister-to-resister transition. Specifically, we focused on AXL because this receptor, along with its ligand, growth arrest–specific protein 6 (GAS6), is upregulated in lung cancer cells that acquire reversible resistance to TKIs (19). Rather than functioning as an oncogenic driver, AXL promotes stemness and motility (20). Its ligand is similarly unique: It binds to phosphatidylserine that is externalized on apoptotic cells, thereby allowing AXL to sense stress and potentially trigger endogenous mutators. Focusing on AXL, we demonstrate that, conceptually similar to antibiotic-treated bacteria, tumor cells evade drugs by mobilizing endogenous AXL-driven mutators that can be blocked by applying drugs within the narrow window of the persister-to-resister transition.

RESULTS

High GAS6 Characterizes Cycling Persisters and Residual Patient Disease, Whereas Activation of AXL Is Essential for Resistance to EGFR Inhibitors

The ability of cancer cells to evolve resistance might be predetermined (21). To study this, we isolated single-cell subclones of PC9 lung cancer cells (E746_A750 del-EGFR) in the absence of drugs and exposed each subclone to erlotinib. Note that TKI treatment lasted either 3 or 14 days, but clones that displayed relatively high persistence after 3 days remained so after 2 weeks. A surprisingly wide and reproducible variation in persister cell percentages (Supplementary Fig. S1A and S1B) led us to sequence RNA from subclones with the lowest and subclones with the highest persistence. Importantly, all clones displayed the founder EGFR's driver mutation but none displayed the resistance-conferring mutation T790M. However, one low-persistence clone expressed V689L (22). Differential expression analysis identified *GAS6* as the most significantly overexpressed gene in the high-persistence subclones (Fig. 1A). Because AXL expression was slightly higher in these clones (Supplementary Fig. S1C), we treated cells with osimertinib and analyzed RNA using PCR, which confirmed the early upregulation of GAS6 and relatively late and weaker upregulation of AXL (Supplementary Fig. S1D). In addition, we detected secreted GAS6 in the medium of treated cells (Supplementary Fig. S1E). Next, we examined the association with persister cell proliferation by reanalyzing data from PC9 cells transduced by Watermelon, a lentiviral library that permits tracing proliferative states (23). According to the results, GAS6 was highly enriched in cycling persisters relative to noncycling persisters (Fig. 1B; $P = 0$). When we referred to single-cell RNA-sequencing (RNA-seq) data from a clinical trial that evaluated osimertinib (NCT03433469), it turned out that treatment-naïve (TN) patients, as well as patients who experienced progressive disease (PD), displayed low or undetectable GAS6. In contrast, the majority of the residual disease (RD) group displayed high GAS6 (Fig. 1C). This suggested the binding of GAS6 to the cognate RTK, either AXL or MERTK, permits persister cell proliferation. Support for this notion came from an analysis of a recently published patient data set (24) showing that AXL upregulation and TKI treatment were positively correlated (Fig. 1D; $P = 8.2 \times 10^{-9}$). Altogether, these observations raised the possibility that the GAS6–AXL axis is associated with cycling persisters.

In line with the clinical data, phosphorylation of AXL increased following treatment of PC9 cells with TKIs (Supplementary Fig. S1F and S1G). Reverse-phase protein array (RPPA) analyses confirmed adaptive upregulation of AXL and additional RTKs (Supplementary Fig. S1H), and cytometry validated that the induced AXL molecules reached the cell surface (Supplementary Fig. S1I). Functionality was addressed by applying gain- and loss-of-function strategies. Two clones of AXL-overexpressing (OX) PC9 cells were established, along with empty vector (EV) control cells (Supplementary Fig. S1J and S1K). Similarly, we used CRISPR–Cas9 to establish derivatives devoid of AXL (KO1 and KO2; Supplementary Fig. S1L and S1M), and control guide RNA cells (denoted PC9-WT). We then incubated OX1, KO1, and the respective controls with TKIs and 9 days later quantified cell survival. As reported (9), very few cells survived this treatment. Nevertheless, AXL overexpression increased this fraction (Fig. 1E), and fewer AXL-depleted cells survived treatment (Fig. 1F). These *in vitro* data were further evidence that the GAS6–AXL axis supports the survival of DTP cells.

Figure 1. GAS6 expression characterizes cycling persisters; upregulation of the cognate receptor AXL is essential for resistance. **A,** Single-cell PC9 subclones were established in the absence of drugs. Following treatment with erlotinib, we obtained RNA-seq data from each subclone. The volcano plot presents genes that are differentially expressed in the 8 highest versus the 8 lowest persistence subclones. Red dots mark genes exceeding two cutoffs: *P* value and change in expression. **B,** Shown are GAS6 expression levels in Watermelon-transduced PC9 cells treated with osimertinib for the indicated time intervals. Day 14 persisters were sorted into 3 groups according to their cycling status. **C,** Single-cell GAS6 expression levels in human non–small cell lung cancer tumors clinically characterized as treatment naïve (TN), residual disease (RD), and progressive disease (PD; 457, 557, and 1,088 cells per group, respectively). Data from NCT03433469. **D,** Single-cell RNA-seq data (29) from TN (21 samples), RD (16 samples), and PD (16 samples) were analyzed for AXL transcripts. Each dot represents a single tumor cell. Box-and-whisker plot: center line, median; box limits, upper (third) and lower (first) quartiles; whiskers indicate maximum and minimum values. Y-axis is a $\log_2$ scale (one-way Kruskal–Wallis test). **E** and **F,** AXL-overexpressing (OX; **E**) or AXL-knockout (KO; **F**) PC9 cells, along with the respective control cells, were untreated or treated with TKIs (1 or 3 μmol/L). On day 9, surviving cells were stained and quantified (average ± SD, triplicates, and 3 experiments). **G,** PC9 cells (2×10^6) were subcutaneously implanted in nude mice. When tumors became palpable, mice were randomized into groups (8 or 10 animals per group) that were treated daily with erlotinib (10 mg/kg/day) or osimertinib (5 mg/kg/day). Tumor volumes are presented (average ± SEM). Note that due to ulceration, one animal of the control arm was eliminated. **H,** 3–4 mice from each group shown in **G** were euthanized when tumors reached 1,500 mm^3. Tumors were extracted and subjected to immunoblotting. Tubulin (TUB) served as the loading control. **I** and **J,** AXL-overexpressing PC9 cells (**I**) and AXL-knockout PC9 cells (2×10^6, **J**), along with the respective control cells, were subcutaneously implanted in mice. When tumors became palpable, mice were randomized and treated as in **G**. n.s., not significant. *, $P \leq 0.05$; **, $P \leq 0.01$; ***, $P \leq 0.001$.

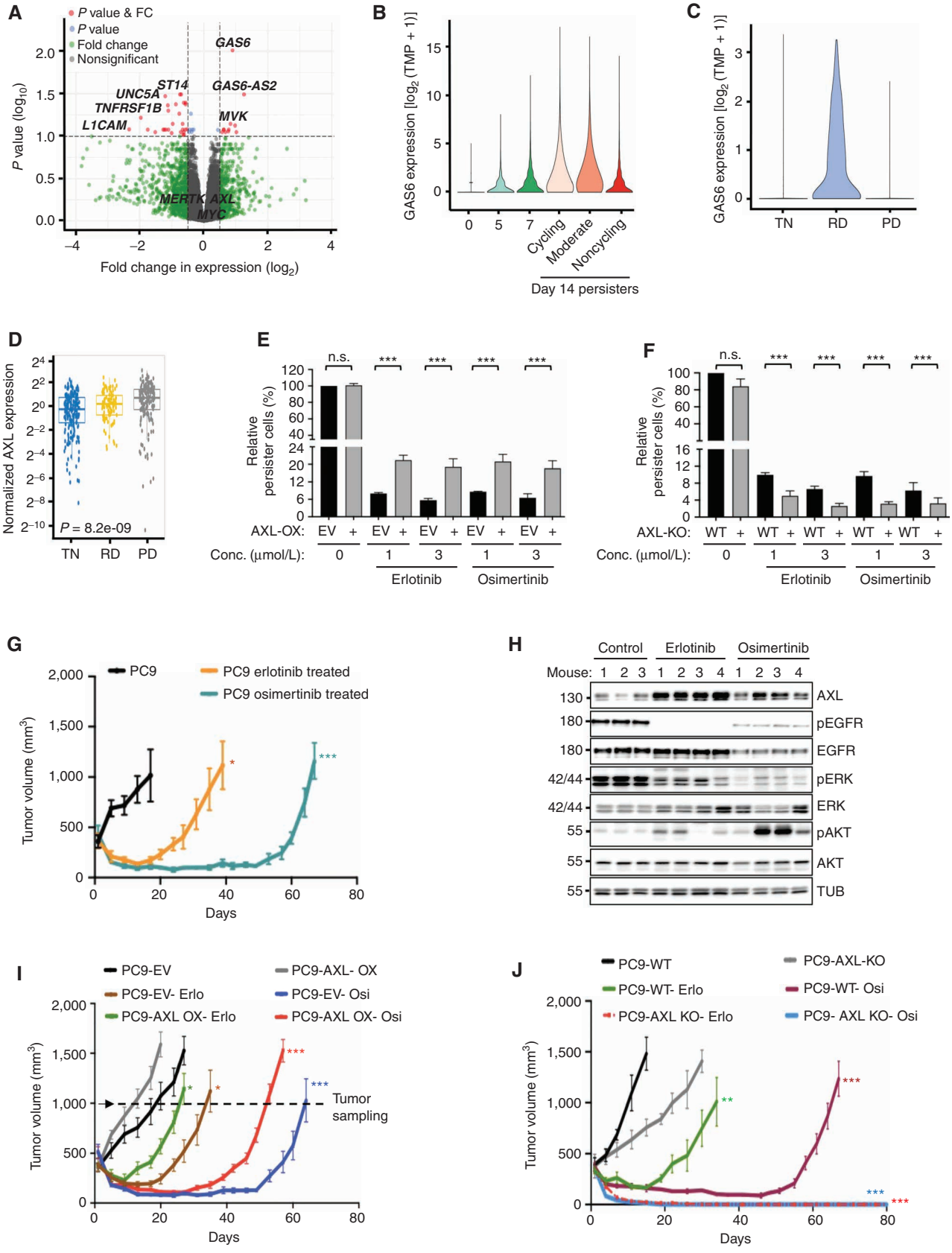
A
P value & FC
P value
Fold change
Nonsignificant
GAS6
GAS6-AS2
ST14
UNC5A
TNFRSF1B
L1CAM
MVK
MERTK AXL MYC
P value (log10)
Fold change in expression (log2)
B
GAS6 expression [log2 (TMP + 1)]
Cycling
Moderate
Noncycling
Day 14 persisters
C
GAS6 expression [log2 (TMP + 1)]
TN
RD
PD
D
Normalized AXL expression
P = 8.2e-09
TN
RD
PD
E
Relative persister cells (%)
n.s.
***
AXL-OX:
EV
Conc. (μmol/L):
Erlotinib
Osimertinib
F
Relative persister cells (%)
AXL-KO:
WT
Conc. (μmol/L):
Erlotinib
Osimertinib
G
PC9
PC9 erlotinib treated
PC9 osimertinib treated
Tumor volume (mm3)
Days
H
Control
Erlotinib
Osimertinib
Mouse: 1 2 3 1 2 3 4 1 2 3 4
AXL
pEGFR
EGFR
pERK
ERK
pAKT
AKT
TUB
I
PC9-EV
PC9-AXL- OX
PC9-EV- Erlo
PC9-EV- Osi
PC9-AXL OX- Erlo
PC9-AXL OX- Osi
Tumor sampling
Tumor volume (mm3)
Days
J
PC9-WT
PC9-AXL-KO
PC9-WT- Erlo
PC9-WT- Osi
PC9-AXL KO- Erlo
PC9- AXL KO- Osi
Tumor volume (mm3)
Days

Although adaptive AXL activation has been previously reported (14, 16), its contribution to drug resistance has remained incompletely understood. We therefore implanted PC9 cells in mice and, once tumors became palpable, started daily TKI treatments (Fig. 1G). Analogous to clinical scenarios, all tumors initially regressed but later relapsed. Posttreatment analysis detected the upregulation of AXL, as well as sporadic ERK inactivation and AKT activation (Fig. 1H). Next, the experiment was repeated using OX (Fig. 1I) and KO cells (Fig. 1J). As shown, OX cells displayed earlier emergence of resistance, and, strikingly, TKI-treated KO cells showed no relapses at all. This absolute dependence of relapses on AXL suggested that adaptive activation of the GAS6–AXL axis permits the emergence of resistance. In conclusion, the GAS6–AXL axis is activated in response to TKIs, and its ability to support the proliferation of persister cells is essential for the emergence of resistance.

EGFR Inhibitors Increase DNA Breaks and Reduce Homologous Recombination Proficiency, but AXL Opposes These Effects

Assuming that tumors acquire resistance by mobilizing AXL-dependent endogenous mutators, we began by testing the effects of AXL on DNA breaks. As expected, exposure of PC9 cells to EGFR inhibitors increased apoptosis and reduced viability, whereas AXL overexpression enhanced viability and inhibited apoptosis (Fig. 2A and B). Analysis of KO cells supported the ability of AXL to increase viability and inhibit apoptosis (Supplementary Fig. S2A and S2B). The TKIs also increased γH2A.X, which marks DNA double-strand breaks (DSB), but AXL inhibited rather than enhanced this effect (Fig. 2C and D; Supplementary Figs. S2C–S2G and S3A). Using the alkaline comet assay, which monitors DNA breaks by measuring comets' heads and tails, we inferred that TKIs induce DNA fragmentation but AXL attenuates this response (Fig. 2E; Supplementary Fig. S3B). Congruent with the ability of reactive oxygen species (ROS) to induce DSBs, TKIs increased and AXL decreased ROS production (Fig. 2F; Supplementary Fig. S3C). Next, we used BLISS to profile DSBs on a genome-wide scale (25). Although similar break patterns were observed in gene bodies and promoter regions, TKI treatments increased whereas AXL reduced break densities (Fig. 2G). Thus, TKIs elevate ROS and, accordingly, increase DNA breaks, but AXL inhibits these effects. Lastly, evaluating homologous recombination (HR) proficiency by using a plasmid, pDRGFP/pCBASce-I (26) uncovered marked reductions in HR proficiency post TKI treatment, but we observed no consistent modulation by AXL (Fig. 2H; Supplementary Fig. S3D).

AXL Facilitates TKI-Induced Upregulation of RAD18 and Error-Prone DNA Polymerases

Because AXL inhibits rather than induces DNA breaks, we turned to study alternative mutators. Replication fidelity is influenced by mutagenic DNA polymerases specialized in translesion synthesis (TLS; ref. 27). TLS polymerases collaborate with RAD18 and enhance damage tolerance at the expense of replication fidelity (28). To examine AXL involvement, we extracted AXL-overexpressing tumors while they were relapsing in TKI-treated animals. This unveiled AXL-independent reduction in RAD51 and BRCA1, which function in the repair of DNA DSBs by HR (Fig. 3A). In contrast, RAD18 and three error-prone TLS polymerases (eta, iota, and kappa) underwent upregulation in TKI-treated tumors only if they overexpressed AXL. To unravel relevant mechanisms, we subjected TKI-induced persister cells to qPCR and immunoblotting (Fig. 3B; Supplementary Fig. S4A), which detected late activation of AXL and concurrent transcriptional upregulation of RAD18 and 7 low-fidelity polymerases. In parallel, 4 high-fidelity polymerases and several HR and mismatch-repair (MMR) genes underwent downregulation. Treating H1975 cells (L858R and T790M EGFR) indicated that, similar to PC9 cells, RAD18 was upregulated in H1975 cells treated with osimertinib. However, we observed no induction of RAD18 in erlotinib-treated H1975 cells (Supplementary Fig. S4B), in agreement with the known resistance of these cells to first-generation TKIs.

Next, we attempted to quantify genomic alterations by comparing the whole-exome sequences (WES) of untreated and TKI-treated tumors. For this, CD1-nu/nu mice were subcutaneously inoculated with PC9 cells (3×10^6), either AXL overexpressors or control cells. When tumors became palpable, mice were randomized into groups that were treated daily with osimertinib (5 mg/kg/day) or erlotinib (50 mg/kg/day). Once relapsing tumors reached 1,000 mm^3, they were excised and DNA was isolated for WES analysis. This analysis detected TKI-induced 2.31-fold (erlotinib) and 2.37-fold (osimertinib) increases in all base alterations, including transitions and transversions. Importantly, larger increases (2.42- and 2.52-fold) were found in the respective AXL-overexpressing tumors (Supplementary Excel File S1). Next, we obtained data from 8 clinical samples for which both RNA-seq and WES information were available (29). The tumor mutation burden was computed for each sample, and the Pearson correlation coefficient was calculated. This revealed that AXL expression level and tumor mutational burden were positively correlated ($r = 0.38$). To ascertain the correlation,

Figure 2. TKIs induce DNA breaks but AXL restrains DNA fragmentation. Control (EV) and AXL-overexpressing (OX) PC9 cells were used. **A,** Cells were incubated for 72 hours with TKIs (10 nmol/L), and viability was determined (means ± SD, triplicates). **B,** Cells were treated for 48 hours with TKIs (1 μmol/L), and the fractions undergoing early/late apoptosis were determined (means ± SD, triplicates). **C,** Cells were treated as in **B**, and cell extracts were probed for the indicated proteins using immunoblotting and quantification (underneath numbers). **D,** Cells grown on coverslips were treated as in **A**. Fixed cells were stained for γH2A.X, actin, and DAPI, and images were captured using a confocal microscope (images are not shown). For the quantification of γH2A.X foci, we randomly selected 30 cells from each sample. The dot plot depicts average counts (lines) of foci per nucleus. Each dot corresponds to a single cell. The results represent means (± SD) from three experiments. **E,** The indicated cells were incubated with TKIs (1 μmol/L) for 24 hours. DNA damage was estimated according to the means of 40 comets (see Supplementary Fig. S3B) scored per condition. Results represent means (±SD) from 3 experiments. **F,** Cells were treated for 48 hours as in **A** and ROS levels were assayed. Data are means (±SD) from three experiments. **G,** OX or control PC9 cells (10^6) were incubated for 48 hours with osimertinib (1 μmol/L), and DNA libraries of DSBs were prepared using BLISS. This step was followed by nucleotide sequencing. DSB counts were normalized across the whole genome, and relative abundance of breaks at gene bodies (top) or promoters (bottom) were measured. Data are means ± SD. **H,** Cells stably expressing pDRGFP were transfected with pCBASce-I and then treated as in **A**, prior to flow cytometry. Mock transfection was used for normalization. Quantification of relative HR capacities is shown (means ± SD, triplicates). n.s., not significant. *, $P \le 0.05$; **, $P \le 0.01$; ***, $P \le 0.001$.

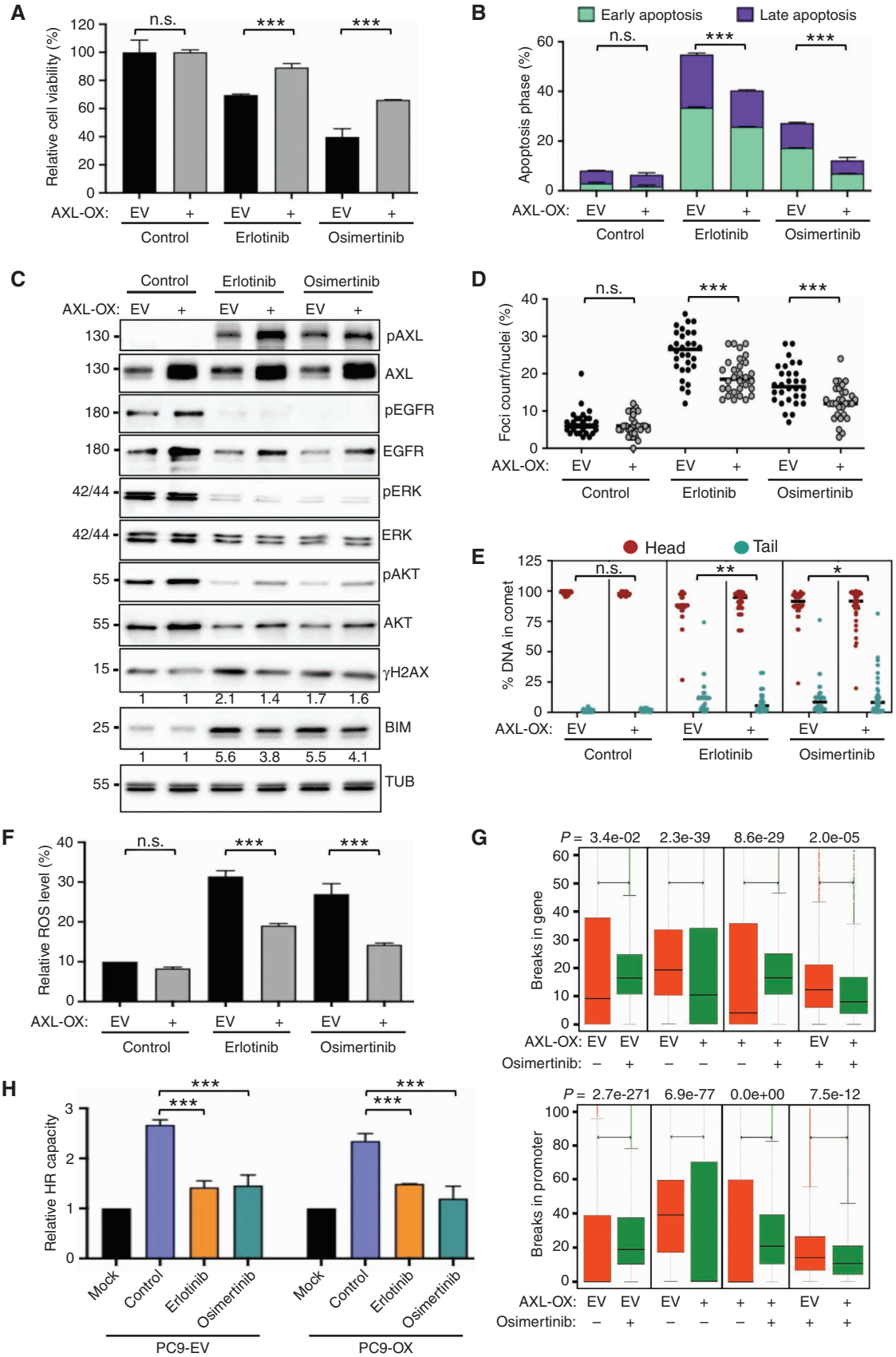
A
Relative cell viability (%)
n.s.
***
***
AXL-OX: EV + EV + EV +
Control
Erlotinib
Osimertinib
B
Early apoptosis
Late apoptosis
Apoptosis phase (%)
n.s.
***
***
AXL-OX: EV + EV + EV +
Control
Erlotinib
Osimertinib
C
Control
Erlotinib
Osimertinib
AXL-OX: EV + EV + EV +
pAXL
AXL
pEGFR
EGFR
pERK
ERK
pAKT
AKT
γH2AX
1 1 2.1 1.4 1.7 1.6
BIM
1 1 5.6 3.8 5.5 4.1
TUB
D
Foci count/nuclei (%)
n.s.
***
***
AXL-OX: EV + EV + EV +
Control
Erlotinib
Osimertinib
E
Head
Tail
% DNA in comet
n.s.
**
*
AXL-OX: EV + EV + EV +
Control
Erlotinib
Osimertinib
F
Relative ROS level (%)
n.s.
***
***
AXL-OX: EV + EV + EV +
Control
Erlotinib
Osimertinib
G
P = 3.4e-02 2.3e-39 8.6e-29 2.0e-05
Breaks in gene
AXL-OX: EV EV EV + + + EV +
Osimertinib: – + – – – + + +
P = 2.7e-271 6.9e-77 0.0e+00 7.5e-12
Breaks in promoter
AXL-OX: EV EV EV + + + EV +
Osimertinib: – + – – – + + +
H
Relative HR capacity
***
***
***
***
Mock
Control
Erlotinib
Osimertinib
Mock
Control
Erlotinib
Osimertinib
PC9-EV
PC9-OX

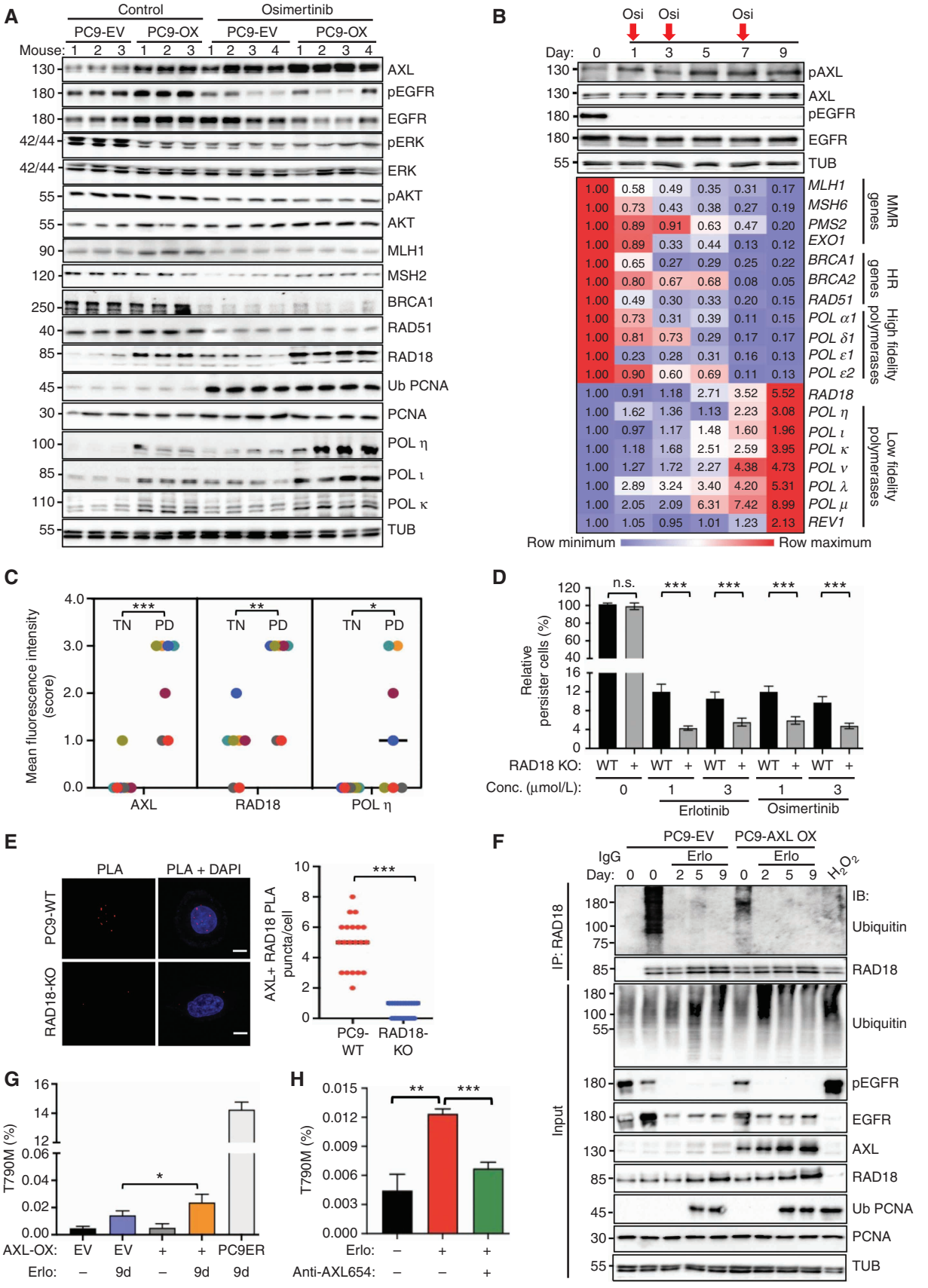
A
Control
Osimertinib
PC9-EV
PC9-OX
Mouse: 1 2 3 1 2 3 1 2 3 4 1 2 3 4
AXL
pEGFR
EGFR
pERK
ERK
pAKT
AKT
MLH1
MSH2
BRCA1
RAD51
RAD18
Ub PCNA
PCNA
POL η
POL ι
POL κ
TUB
B
Osi Osi Osi
Day: 0 1 3 5 7 9
pAXL
AXL
pEGFR
EGFR
TUB
MLH1 MSH6 PMS2 EXO1 — MMR genes
BRCA1 BRCA2 RAD51 — HR genes
POL α1 POL δ1 POL ε1 POL ε2 — High fidelity polymerases
RAD18 POL η POL ι POL κ POL ν POL λ POL μ REV1 — Low fidelity polymerases
Row minimum
Row maximum
C
Mean fluorescence intensity (score)
TN PD
AXL
RAD18
POL η
D
Relative persister cells (%)
n.s.
RAD18 KO: WT + WT + WT + WT + WT +
Conc. (μmol/L): 0 1 3 1 3
Erlotinib
Osimertinib
E
PLA
PLA + DAPI
PC9-WT
RAD18-KO
AXL+ RAD18 PLA puncta/cell
PC9-WT
RAD18-KO
F
PC9-EV
PC9-AXL OX
IgG
Erlo
Day: 0 0 2 5 9 0 2 5 9
H2O2
IP: RAD18
IB:
Ubiquitin
RAD18
Input
Ubiquitin
pEGFR
EGFR
AXL
RAD18
Ub PCNA
PCNA
TUB
G
T790M (%)
AXL-OX: EV EV + + PC9ER
Erlo: – 9d – 9d 9d
H
T790M (%)
Erlo: – + +
Anti-AXL654: – – +

we analyzed another clinical data set (24). The analysis of paired samples from six patients with lung cancer (before and after treatment with osimertinib) confirmed that AXL transcript levels and the number of tumor mutations were significantly correlated in this data set ($P = 0.047$; Supplementary Fig. S4C). In conclusion, the integration of data from patients' tumors and from animal xenografts confirmed a statistically significant association between mutation burden and the expression of AXL.

Clinical relevance was further examined by analyzing RNA-seq data from a group of 18 $EGFR^+$ patients, who were categorized by imaging as having RD (29). The resultant correlation matrix is shown in Supplementary Fig. S4D. As predicted, the abundance of AXL's mRNA correlated positively with the low-fidelity polymerase lambda and negatively with two HR genes (*BRCA2* and *BRCA1*) and several high-fidelity DNA polymerases. However, the mutagenic polymerase REV1 and two MMR genes negatively and positively correlated with AXL, respectively. Hence, we approached these alterations from a different angle and performed two sets of IHC analyses of paired biopsies (pre- and post-TKI treatment). Analysis of the first set (7 patients; Fig. 3C; Supplementary Fig. S4E) validated upregulation of AXL, RAD18, and polymerase eta following TKI treatment. Prior to the second analysis, we stained AXL in paired biopsies from 12 patients. Cases with the three lowest and three highest AXL upregulation at the PD state were stained for RAD18 and DNA polymerase eta (Supplementary Fig. S4F and S4G). Once again, the results confirmed treatment-induced upregulation of nuclear RAD18, but this was limited to the AXL-high specimens. Similarly, the AXL-low group showed no association whatsoever between TKI treatment and polymerase eta, whereas the AXL-high group displayed a clear trend toward posttreatment upregulation of the polymerase. In summary, data from DTP cells, animal models, and patient samples disclosed TKI-induced and AXL-facilitated upregulation of RAD18 and TLS polymerases.

AXL Binds with and Activates RAD18 by Means of Neddylation

RAD18-mediated monoubiquitination of proliferating cell nuclear antigen (PCNA) is critical for TLS (30): In response to damage, Ub_1-PCNA recruits mutagenic polymerases to stalled replication forks (31). To study these interactions, we established PC9 derivatives lacking RAD18 (RAD18-KO). As expected, these cells gave rise to fewer DTPs (Fig. 3D). Next, we examined whether AXL and RAD18 form complexes, a possibility previously raised on the basis of bulk mass spectrometry (ref. 32; https://thebiogrid.org/107036/summary/homo-sapiens/axl.html). Both coimmunoprecipitation (Supplementary Fig. S5A) and proximity ligation assays (PLA; Fig. 3E) confirmed physical interactions and detected the complexes in nuclei.

Because neddylation of RAD18 inhibits its ubiquitination and enhances interactions with PCNA (33), we predicted that AXL regulates this process. Overexpression of AXL did indeed enhance neddylation (Supplementary Fig. S5B) and reduced ubiquitination of RAD18 (Supplementary Fig. S5C). In addition, when assayed in DTPs, both TKI treatment and AXL overexpression reduced and increased ubiquitination of RAD18 and PCNA, respectively (Fig. 3F). The increased mutagenesis predicted by these observations was investigated by subjecting DTP cells to digital PCR analysis. As shown in Fig. 3G, erlotinib enhanced the abundance of T790M, the most prevalent secondary mutation, and AXL overexpression further augmented this effect. Reciprocally, incubating DTP cells with an anti-AXL antibody significantly reduced the abundance of the T790M mutation (Fig. 3H). These observations raised the possibility that the kinase inhibitor and AXL upregulation have led to *de novo*, newly acquired secondary mutations. However, one cannot rule out that these treatments were selected for preexisting, relatively rare T790M-expressing clones, as was previously described (34).

Taken together, these observations proposed that AXL activates RAD18 by means of enhanced neddylation and reduced ubiquitination. Several control experiments are consistent with the possibility that the resulting RAD18's active state initiates ubiquitination of PCNA, thereby promoting adaptive mutability and the emergence of T790M. First, by constructing deletion mutants, we inferred that AXL's cytoplasmic domain, rather than the extracellular domain, binds with RAD18 (Supplementary Fig. S5D and S5E). Second, AXL-KO cells lost two DTP characteristics: upregulation of RAD18 and upregulation of mutation-prone DNA polymerases (Supplementary Fig. S5F). Third, because mutation rates relate to the number of cell divisions, we addressed whether AXL-overexpressing cells divide faster than parental PC9 cells. However, the results we obtained using two different methods (Supplementary Fig. S5G and S5H) indicated that high AXL levels confer only limited effects on cell proliferation rates.

Figure 3. AXL overexpression augments TKI-induced upregulation of both RAD18 and TLS polymerases and enhances the emergence of the T790M mutation. **A,** PC9 tumors were extracted at the marked timing (see Fig. 1I) and immunoblotted as indicated. **B,** PC9 cells were treated with osimertinib (1 μmol/L), or DMSO, for 0–9 days. Red arrows indicate TKI replenishments. Proteins and RNA were subjected to immunoblotting and real-time PCR, respectively. **C,** Pairs of tumor slices were obtained from 7 patients, before and after treatment with osimertinib. The corresponding slides were incubated with primary antibodies specific to AXL, RAD18, and DNA polymerase eta. Slices from the same patient are indicated with a distinct color. Immunoreactivities were evaluated, and scores were generated (two-way ANOVA with the Sidak multiple comparisons test). **D,** Control and RAD18 KO cells were treated for 9 days with TKIs. Fractions of surviving DTPs from 3 experiments are shown. **E,** Naïve and RAD18-knockout PC9 cells were probed using anti-AXL or anti-RAD18 antibodies. Thereafter, the cells were processed for proximity ligation analysis (red dots). Representative images and PLA quantification are shown. Scale bars, 20 μm. **F,** Cells were treated for 2–9 days with erlotinib (1 μmol/L) or H_2O_2 (40 μmol/L). Extracts were subjected to immunoprecipitation with an anti-RAD18 (or control) antibody and immunoprecipitates were immunoblotted (IB) as indicated. **G,** Naïve and AXL-overexpressing cells, along with PC9ER cells (erlotinib resistant), were treated with erlotinib (1 μmol/L). Genomic DNA was isolated after 9 days and the T790M point mutation was assayed using digital PCR. Shown are fractions of T790M in cellular DNA. Data are means ± SEM (4 experiments). **H,** PC9 cells were treated with erlotinib (1 μmol/L) and an anti-AXL monoclonal antibody (20 μg/mL), as indicated. Genomic DNA was isolated after 9 days and the T790M point mutation was assayed using digital PCR. Shown are fractions of T790M in cellular DNA. Data are means ± SEM (4 experiments). *, $P \le 0.05$; **, $P \le 0.01$; ***, $P \le 0.001$.

AXL Enhances Purine Metabolism, Which Might Further Augment Mutagenesis

Next, we sequenced RNA from naïve and AXL-KO cells and performed pathway enrichment analysis (Fig. 4A; Supplementary Excel File S2). This uncovered two groups of differentially regulated transcripts; the primary one is involved in metastasis and the secondary one in nucleotide metabolism, mainly the interconnected purine, histidine, and glutamine pathways. Because high-fidelity DNA replication depends on the pools of dNTP (35) and it influences both proofreading (36) and mutator phenotypes due to unbalanced purine/pyrimidine ratios (37, 38), we first focused on the metabolic alterations. PCR analysis confirmed altered transcription of genes engaged in purine metabolism (Supplementary Fig. S6A), including PPAT and PAICS, which we validated by immunoblotting (Supplementary Fig. S6B). To directly validate metabolic effects, we subjected extracts of KO and control cells to global small-molecule mass spectrometry (Fig. 4B; Supplementary Excel File 3). Among the top differential hits were metabolites in the *de novo* purine synthesis pathway, such as guanosine 5′-monophosphate (GMP) and inosine 5′-monophosphate (IMP), which were significantly decreased, along with increased levels of their precursors, adenine, guanine, and adenosine. Targeted mass spectrometry confirmed reduced levels of IMP, adenosine 5′-monophosphate (AMP), and GMP (Supplementary Fig. S6C) and, conversely, increased levels of these metabolites in AXL-overexpressing cells (Supplementary Fig. S6D).

To ascertain that *de novo* purine synthesis is controlled by AXL, we used targeted tandem mass spectrometry (LC/MS-MS) to measure the relative flux of stable isotope-labeled [amide-15N]glutamine, which is incorporated into the purine ring at two positions. Purine biosynthesis rates were evaluated by measuring isotope incorporation into IMP, as described (39). This analysis showed that the doubly labeled form of IMP, m+2, was dominant after incubating naïve PC9 cells with [amide-15N]glutamine (Fig. 4C). Although m+1 did not significantly change in KO cells, these cells displayed reduced IMP m+2, in line with the ability of AXL to accelerate *de novo* purine synthesis. When the incorporation of 13C arising on [U-13C]glucose into purines was compared with control cells, KO cells displayed lower m+2, m+6, m+7, and m+8 of the mono-, di-, and trinucleotides, along with higher fractions of m+0 (Fig. 4D), further indicating that AXL can boost purine synthesis. Additional analyses attributed the underlying mechanism to the ability of AXL to activate MYC, a well-characterized AXL transcriptional target (40): First, AXL overexpression stimulated the MYC promoter (Fig. 4E), whereas an MYC inhibitor reduced PPAT and PAICS (Supplementary Fig. S6E), and both AXL and MYC activated the respective reporters (Fig. 4F). Second, colony formation assays comparing the effect of osimertinib and inhibitors that directly or indirectly target the purine synthesis pathway showed that all three drugs inhibited colony formation, and these effects were enhanced when AXL-ablated cells were examined (Supplementary Fig. S6F). Lastly, PPAT, PAICS, and additional purine synthesis enzymes exhibited downregulation at both the mRNA and protein levels in the context of DTP cells (Fig. 4G and H).

Taken together, these results indicated that, in response to TKIs, AXL levels are enhanced and activate MYC, which might increase purine mutational bias (PuMB; ref. 41). Consistent with this scenario, analysis of PuMB signatures in the WES data we obtained from control and TKI-treated tumors grown in animals implied that TKIs are able to upregulate PuMB (Supplementary Fig. S6G). In addition, we found that high PuMB scores are associated with tumors harboring mutant EGFR, rather than WT-EGFR (Fig. 4I). Similarly, regression analysis of a small cohort of patients for whom both cancer cell single-cell RNA-seq data and tumor WES data were available (24) showed a trend toward a positive correlation between AXL expression and PuMB (Fig. 4J). Furthermore, when lung cancers harboring *RAS* mutations, which might depend on coactivation of MYC (42), were compared with cancers with *EGFR* mutations, we noted that the *EGFR* group displayed significantly higher PuMB (Fig. 4K). Congruent with the involvement of the AXL-to-MYC axis, the core MYC expression signature (43) correlated positively with high AXL levels in the lung adenocarcinoma data set of The Cancer Genome Atlas (TCGA; Fig. 4L). In conclusion, treatments making use of TKIs likely activate AXL and MYC, causing an imbalance in nucleotide metabolism and increasing adaptive mutability.

High expression of AXL and differential expression of GAS6 predict poor survival of patients with lung cancer (44). In line with this, AXL-KO cells exhibited altered expression of genes involved in migration/proliferation (Fig. 4A), along with reduced DNA synthesis and increased markers of senescence (Supplementary Fig. S6H–S6K). KO cells also

Figure 4. AXL induces purine metabolism and increases PuMB. **A,** RNA from PC9 cells and AXL-KO cells was sequenced, and differentially expressed genes were subjected to KEGG Pathway Enrichment analysis. **B,** A waterfall plot depicting fold changes in metabolite abundance in AXL-KO relative to PC9-WT (control) cells. Metabolites were rank-ordered, and specific compounds are indicated (assays performed in triplicates). **C,** Fractional labeling of IMP in PC9-KO and PC9-WT (control) cells using [amide-15N]glutamine and 24 hours of incubation. **D,** Fractional labeling of purines determined in AXL-KO and PC9-WT cells incubated for 24 hours with [U-13C]glucose (means ± SD; 3 experiments). **E,** An AXL expression vector and *MYC* promoter reporter plasmid were transfected into HEK293 cells. Renilla was used as a control. Luminescence reading was taken 48 hours later. **F,** *PPAT* and *PAICS* promoter reporter plasmids were transfected into HEK293 cells, along with AXL and MYC vectors. Luminescence readings (means ± SD; 3 experiments) were normalized to a GAPDH reporter. **G,** PC9 cells were treated with osimertinib (1 μmol/L) or DMSO for the indicated time intervals. RNA was isolated and subjected to real-time PCR using primers corresponding to the indicated transcripts. **H,** PC9 cells were either untreated or treated for 9 days with TKIs at the indicated concentrations. Control cells were treated with DMSO. The indicated proteins were detected using immunoblotting. Tubulin served as the gel loading control. **I,** PuMB was analyzed in the TCGA lung adenocarcinoma data set ($n = 506$ patients) and presented versus EGFR's mutational status. **J,** A cohort of 10 treatment-naïve patients, for whom both tumoral single-cell RNA-seq data and tumor whole-exome sequencing data were available, was analyzed for AXL expression and PuMB. Dots show individual data points and the diagonal represents a regression line. **K,** The status of AXL expression level and presence of EGFR or RAS mutations in the TCGA data set are shown. **L,** A core MYC gene-expression signature was analyzed against the level of AXL expression in the cohort of 506 patients. ***, $P \leq 0.001$.

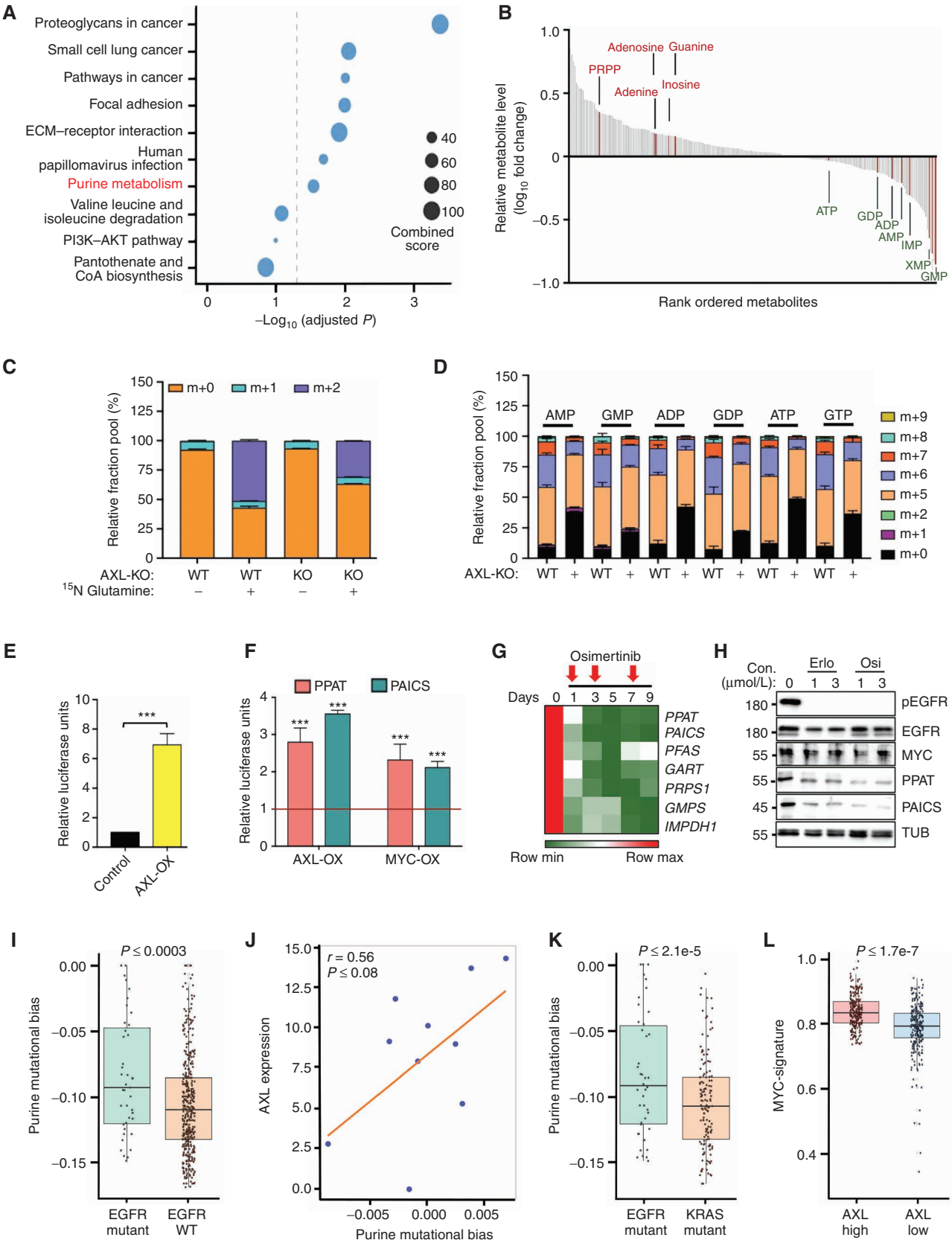
A
Proteoglycans in cancer
Small cell lung cancer
Pathways in cancer
Focal adhesion
ECM–receptor interaction
Human papillomavirus infection
Purine metabolism
Valine leucine and isoleucine degradation
PI3K–AKT pathway
Pantothenate and CoA biosynthesis
40
60
80
100
Combined score
0
1
2
3
−Log10 (adjusted P)
B
Relative metabolite level (log10 fold change)
1.0
0.5
0
−0.5
−1.0
Adenosine
Guanine
PRPP
Adenine
Inosine
ATP
GDP
ADP
AMP
IMP
XMP
GMP
Rank ordered metabolites
C
Relative fraction pool (%)
150
125
100
75
50
25
0
m+0
m+1
m+2
AXL-KO: WT WT KO KO
15N Glutamine: − + − +
D
Relative fraction pool (%)
AMP
GMP
ADP
GDP
ATP
GTP
m+9
m+8
m+7
m+6
m+5
m+2
m+1
m+0
AXL-KO: WT + WT + WT + WT + WT + WT +
E
Relative luciferase units
***
Control
AXL-OX
F
PPAT
PAICS
Relative luciferase units
***
AXL-OX
MYC-OX
G
Osimertinib
Days 0 1 3 5 7 9
PPAT
PAICS
PFAS
GART
PRPS1
GMPS
IMPDH1
Row min
Row max
H
Con.
Erlo
Osi
(μmol/L): 0 1 3 1 3
180
180
55
55
45
55
pEGFR
EGFR
MYC
PPAT
PAICS
TUB
I
P ≤ 0.0003
Purine mutational bias
0.00
−0.05
−0.10
−0.15
EGFR mutant
EGFR WT
J
r = 0.56
P ≤ 0.08
AXL expression
15.0
12.5
10.0
7.5
5.0
2.5
0.0
−0.005
0.000
0.005
Purine mutational bias
K
P ≤ 2.1e-5
Purine mutational bias
0.00
−0.05
−0.10
−0.15
EGFR mutant
KRAS mutant
L
P ≤ 1.7e-7
MYC-signature
1.0
0.8
0.6
0.4
AXL high
AXL low

displayed relatively slow tumor growth and severely reduced ability to colonize lungs following mouse tail-vein injection (Supplementary Fig. S6L–S6N). In summary, our results attribute two important roles to AXL: a master regulator of purines and mutability, and a promoter of metastasis.

A New Anti-AXL Antibody Persistently Inhibits Resistance to Osimertinib

Based on the finding that AXL facilitates mutator phenotypes, we generated anti-AXL mAbs. One antibody in particular, mAb654, was selected for its inhibition of pAKT and DNA synthesis (Supplementary Fig. S7A and S7B). Following a report that combining TKIs and cetuximab, an anti-EGFR mAb, delayed relapses in drug-resistant models (45), we tested various combinations of cetuximab, osimertinib, and mAb654. Unlike the ~50% viability observed with PC9 and H1975 cells treated with osimertinib, each mAb only weakly affected viability (Supplementary Fig. S7C and S7D). However, when we combined osimertinib, cetuximab, and mAb654, significantly fewer cells remained viable. This cooperative effect likely relates to the ability of the triplet to enhance apoptosis (Supplementary Fig. S7E) and increase ROS (Supplementary Fig. S7F). Moreover, the triplet downregulated AXL, pAKT, PPAT, RAD18, and several low-fidelity polymerases (Supplementary Fig. S7G). Ultimately, these attributes translated to strong diminution of DTPs (Supplementary Fig. S7H and S7I). Note that similar effects on viability, apoptosis, TLS, and colony formation were observed when using HCC827 and additional EGFR-mutated cell lines (Supplementary Figs. S8A–S8F, S9A, and S9B).

The triplet's ability to nearly eliminate DTPs predicted inhibition of tumor relapses. We therefore implanted PC9 cells in mice and, when tumors became palpable, randomized them into groups that were treated with osimertinib or with mAbs specific to AXL, EGFR, HER2 (trastuzumab), HER3, or MET (Fig. 5A). Assuming that DTPs seed relapses, all treatments were discontinued on day 30, but we kept monitoring all animals. Of the mAbs used, cetuximab best delayed relapses, and when examined *in vitro*, this antibody increased apoptosis and decreased expression of MMR and HR genes (Fig. 5A; Supplementary Fig. S9C; see survival curves in Supplementary Fig. S10A–S10C). Consistent with these observations, when osimertinib-containing doublets were tested, cetuximab + osimertinib achieved the longest delays (Fig. 5B). Therefore, we combined this pair with each of the other antibodies (Fig. 5C). Remarkably, unlike the other triplets, the combination of cetuximab + osimertinib + mAb654 completely abolished relapses. Importantly, we observed similar results when treating H1975 tumors (Fig. 5D; Supplementary Fig. S10D). Despite short treatments (30 days), no relapses were observed more than 4 months later, weakening the possibility that dormant DTPs survived. These observations imply that transient inhibition of the AXL-dependent switch capable of transforming persisters to resisters can cure mice bearing tumor xenografts.

Two approaches were undertaken to verify the durable effect of the relatively short anti-AXL treatment: (i) analyzing patient-derived xenografts (PDX), which better represent tumor heterogeneity, and (ii) testing the impact of blocking AXL in a more clinically relevant model (i.e., preestablished resistance). The first scenario used the TM00193 PDX model and confirmed the ability of the triplet to completely eradicate resistance (Fig. 5E; Supplementary Fig. S10E). Note that due to logistical considerations, several relatively weak drug combinations (e.g., osimertinib plus mAb654) were not tested in the PDX model. According to the second scenario, treatment-naïve PC9 tumors were first established and then treated with osimertinib—conditions under which tumors initially regress but later relapse. Once tumors regained their initial volume, animals were randomized and treated with various combinations of cetuximab, osimertinib, and mAb654. All groups but the one treated with the triplet experienced relapses (Fig. 6A). In contrast, the triplet achieved complete regression and mice remained tumor-free >3 months after cessation of all treatments (Fig. 6B–G; each panel corresponds to one animal). Tumor extracts obtained after short treatments of the PC9 (Supplementary Fig. S11A) and PDX models (Supplementary Fig. S11B) confirmed that the triplet enhanced apoptosis, reduced abundance of proteins involved in TLS, and, as expected, diminished IMP, AMP, and GMP (Supplementary Fig. S11C). Assuming that the *in vivo* efficacy of the triplet is due to inhibition of the persister-to-resister transition, we performed DTP assays (Supplementary Fig. S11D). When singly applied, osimertinib reduced MMR genes, RAD51 and BRCA1, and, in contrast, upregulated RAD18, GAS6, and error-prone TLS polymerases. In a striking difference, the triplet reduced rather than increased the expression of RAD18 and the majority of error-prone polymerases. Taken together, our results established the ability of relatively short anti-AXL treatments to durably overcome both *de novo* and preestablished resistance, which is attributable to blocking the persister-to-resister switch.

In summary, the adaptive response to EGFR TKIs entails upregulation of several RTK pathways, including the GAS6–AXL axis. Preventing this response by ablating AXL reduced DTP numbers and completely prevented tumor relapses. Upregulation of AXL transcripts was associated with two mutator phenotypes: (i) induction of RAD18 and several mutation-prone DNA polymerases, and (ii) activation of MYC, which unbalances nucleotide pools. Mechanistically, both AXL and TKIs activate RAD18 by inducing its neddylation, thereby initiating the DNA polymerase switch. Analyses of patient data confirmed that AXL expression is associated

Figure 5. Combining an anti-AXL antibody and EGFR blockers prevents tumor relapses. **A–C,** PC9 cells (3×10^6) were implanted in CD1-nu/nu mice. When tumors became palpable, mice were randomized into groups of 8 animals that were treated (hatched area) with the indicated antibodies (total dose: 0.2 mg/mouse/injection) once every three days, or daily with osimertinib (5 mg/kg/day). Data are means ± SEM (**A:** single agent, **B:** dual treatments, **C:** triple drug combinations). **D,** H1975 cells (3×10^6) were subcutaneously implanted in CD1-nu/nu mice. When tumors became palpable, mice were randomized into groups of 10 animals each, which were treated for 30 days (hatched area) with the indicated antibodies (total dose: 0.2 mg/mouse/injection), once per 3 days, or with osimertinib (5 mg/kg/day). Mice were euthanized when tumor size reached 1,500 mm^3. **E,** The PDX tumor model TM00193 was implanted in NSG mice. When tumors became palpable, mice were randomized into groups (7 mice per group) that were treated (hatched area) with the indicated antibodies (see **A**) or with osimertinib (10 mg/kg/day). Tumor volumes (averages ± SD) are indicated. CTX, cetuximab; Osi, osimertinib. *, $P \le 0.05$; **, $P \le 0.01$; ***, $P \le 0.001$.

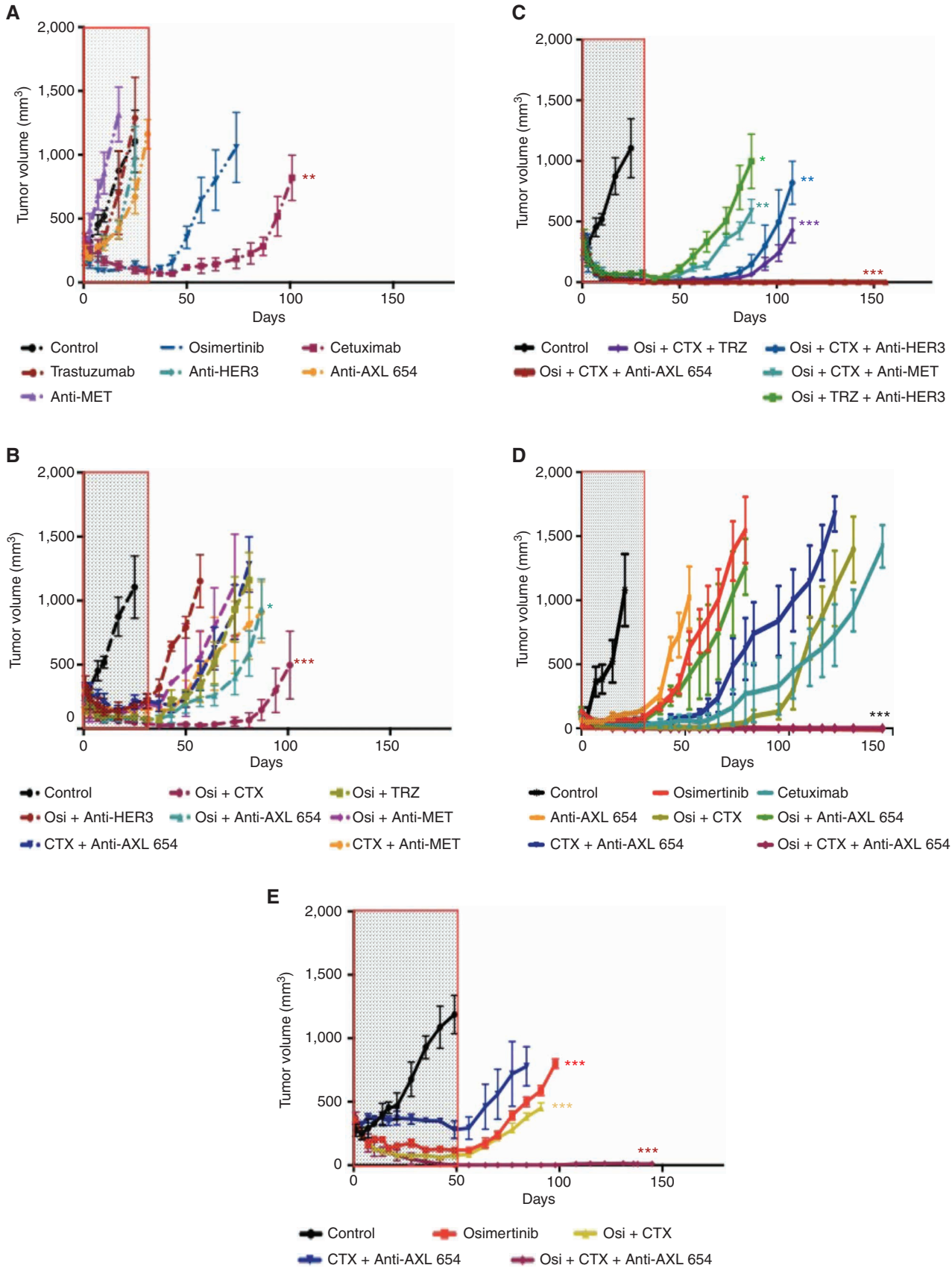
A
Tumor volume (mm3)
2,000
1,500
1,000
500
0
0
50
100
150
Days
**
Control
Osimertinib
Cetuximab
Trastuzumab
Anti-HER3
Anti-AXL 654
Anti-MET
C
Tumor volume (mm3)
Days
*
**
**
***
***
Control
Osi + CTX + TRZ
Osi + CTX + Anti-HER3
Osi + CTX + Anti-AXL 654
Osi + CTX + Anti-MET
Osi + TRZ + Anti-HER3
B
Tumor volume (mm3)
Days
*
***
Control
Osi + CTX
Osi + TRZ
Osi + Anti-HER3
Osi + Anti-AXL 654
Osi + Anti-MET
CTX + Anti-AXL 654
CTX + Anti-MET
D
Tumor volume (mm3)
Days
***
Control
Osimertinib
Cetuximab
Anti-AXL 654
Osi + CTX
Osi + Anti-AXL 654
CTX + Anti-AXL 654
Osi + CTX + Anti-AXL 654
E
Tumor volume (mm3)
Days
***
***
***
Control
Osimertinib
Osi + CTX
CTX + Anti-AXL 654
Osi + CTX + Anti-AXL 654

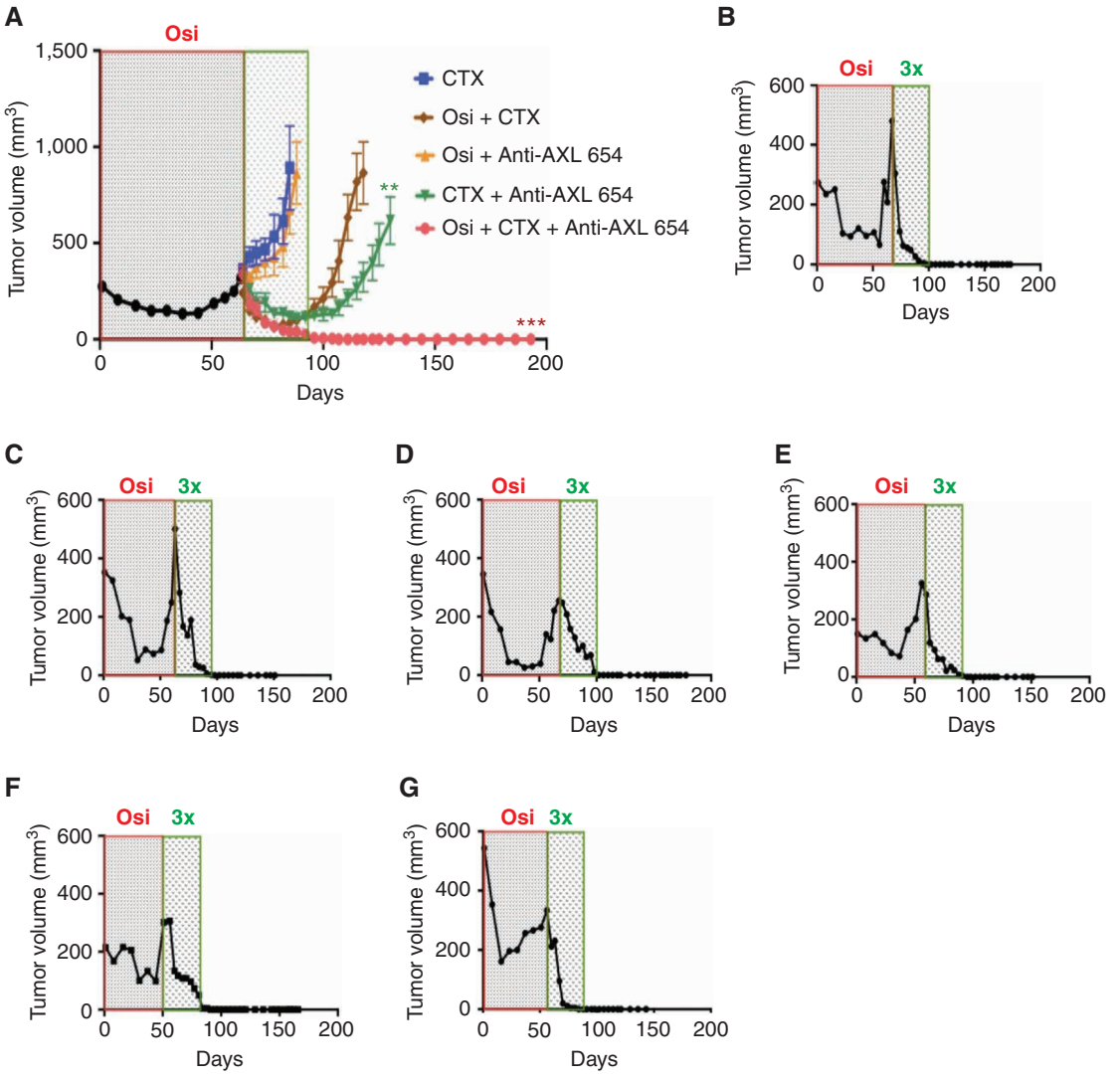

Figure 6. The triple treatment (anti-AXL antibody + cetuximab + osimertinib) inhibits tumors that have already acquired resistance to osimertinib. **A,** PC9 cells (3×10^6) were subcutaneously implanted in CD1-nu/nu mice. When tumors became palpable, mice were treated with osimertinib (5 mg/kg/day) and after tumors regressed and later relapsed (300 mm^3), animals were randomized into groups ($n = 7$) that were treated for 30 days (hatched area) with the indicated drugs. Thereafter, all treatments were stopped, but we continued monitoring the animals. **B–G,** Tumor volumes per individual mice that were initially treated with osimertinib (5 mg/kg/day) and later switched to the triple drug combination (3×). Note that all treatments were terminated once tumors disappeared, but we kept monitoring the animals. CTX, cetuximab, Osi, osimertinib. **, $P \leq 0.01$; ***, $P \leq 0.001$.

with both increased PuMB and high abundance of mutation-prone DNA polymerases. In line with the AXL-dependent conversion of DTP cells to resisters, a triplet containing the new anti-AXL antibody inhibited the mutators and eliminated resistance to TKIs.

DISCUSSION

Similar to bacterial persisters that survive antibiotics by activating the SOS response (46), we report that human lung cancer cells exposed to TKIs activate the GAS6–AXL pathway, which supports the cycling of persisters and initiates the SOS-like response. This reaction mobilizes both transcriptional and nontranscriptional machinery. The nontranscriptional arm entails activation of RAD18 by means of enhanced neddylation and reduced ubiquitination. The transcriptional arm inhibits DNA repair, as well as elevates both low-fidelity DNA polymerases and MYC. The latter controls genes involved in purine synthesis (47). Thus, drug-induced activation of the GAS6–AXL axis unbalances pools of the four dNTPs and triggers genotoxic effects (48). These findings concur with a report that AICAR, the final intermediate of the purine synthesis pathway, is depleted in TKI-resistant cells, whereas the mitochondrial dehydrogenase MTHFD2, which controls purine synthesis, undergoes upregulation (49).

AXL has frequently been linked to acquired resistance to targeted therapies, such as resistance to BRAF (50) and PI3K blockers (51), making this RTK and its direct interaction with RAD18 well positioned to confer resistance by means of

enhancing adaptive mutability. Our finding that forced overexpression of AXL accelerates the emergence of the T790M mutation is consistent with this model, as are previous studies showing that AXL advances the emergence of drug-tolerant lung cancer cells (16). In line with this model, we found that, relative to treatment-naïve lung tumors, the abundance of AXL is increased together with that of RAD18 in tumors isolated from patients who experienced PD following osimertinib treatment. In addition, we showed that AXL levels positively correlate with the mutational loads of patients' tumors, and, reciprocally, downregulation of AXL decreased the occurrence of T790M. The convergence of these pieces of evidence leads us to speculate that AXL overexpression is preceded by the selection of persister clones sharing overexpression of GAS6. This mechanism is reminiscent of the reported autocrine secretion of the hepatocyte growth factor, which accelerates the amplification of the *MET* gene (52).

The observations we made while studying DTPs and using animal models have clinical implications. Beyond the realization that TKI-treated tumors reduce HR and MMR proficiency, and hence expose pharmacologic vulnerabilities, the ability of anti-AXL mAbs to prevent tumor recurrence may warrant clinical testing. We posit that the alignment of anti-AXL treatments with the timing of the persister-to-resister transition might be critical. Indeed, it has been shown that relatively short treatments with IGF1R blockers can inhibit tumor relapses (53). Short and precisely timed treatments might offer another advantage, namely relatively mild adverse effects. As evidence accumulates in support of this concept, temporary treatments based on genetic switches and deep understanding of the mammalian SOS response are more than likely to become a mainstay in medical oncology.

METHODS

Cell Cultures and Reagents

PC9, H1975, HCC827, H2935, and NCI-H3255 cells were procured from ATCC. H1299 cells were grown in 10% RPMI. Cells were cultured for no longer than 3 months and they were routinely checked for *Mycoplasma*. Cell lines were authenticated prior to the experiments. The MYC inhibitor 10058-F4 was obtained from MedChemExpress (MCE). Oligonucleotide primers (Sigma) and the antibodies we used are listed in Supplementary Tables S1 and S2, respectively.

Generation of AXL-Overexpressing Luciferase-Tagged PC9 Cells

Lentiviral particles were produced in HEK293FT cells (Thermo Fisher Scientific, Germany) by cotransfecting lentiviral expression vectors containing the coding region of either AXL (pLX304-AXL) or red firefly luciferase (rwpLX305_IRES_Puro-RedFF), together with second-generation viral packaging plasmids (VSVG; Addgene #14888) and psPAX2 (Addgene #12260). Twenty-four hours after transduction, virus-containing medium was replaced with selection media containing blasticidin for pLX304-AXL and puromycin for rwpLX305_IRES_Puro-RedFF.

In Vitro *Knockout of the Genes Encoding for AXL and RAD18*

The CRISPR–Cas9 system was used to create a double-stranded break next to the Protospacer Adjacent Motif (PAM). The target site was selected using the ENSEMBL database in a way that targeted the transcripts of AXL or RAD18. The selected targets (21 bp) included the PAM sequences in exon 5 (*AXL*) or in exon 2 (*RAD18*).

Generation of Anti-AXL Antibodies

Mouse immunization, fusion between myeloma cells and splenocytes, and the subsequent hybridoma subcloning used standard procedures. A fusion protein combining the extracellular domain of AXL and the Fc domain of a human IgG1 was constructed and used for immunization of mice.

Drug-Tolerant Persister Assays

Drug-sensitive PC9 cells were treated with the relevant TKI, at concentrations exceeding 100 times the established IC_{50} values, for three rounds (each treatment lasted 72 hours). Viable cells remaining attached to the dish at the end of the third round were considered to be DTPs.

HR Assays

Cells were transfected with pDRGFP (Addgene) using Lipofectamine 2000. The plasmid comprises two differentially mutated GFP genes oriented as direct repeats and separated by a drug selection marker (26). Puromycin (5 μg) was used to select stably infected cells. pDRGFP-expressing cells were seeded in 6-well culture plates. On the following day, cells were transfected with the Sce-I–expressing plasmid (pCBASce-I; Addgene). The relative HR capacity was determined by dividing the percentage of GFP-positive cells in the Sce-I–transfected cultures by the percentage of GFP signal in mock control.

WES, Alignment, and Variant Calling

WES was performed by DNA Link (Seoul, Republic of South Korea; https://www.dnalink.com/english/). Reads were mapped to a reference human genome sequence (hg19; NCBI GRCh37) using bwa 0.7.12. Variants were called with GATK's HaplotypeCaller tool 3.5. To filter potential errors, GATK's Variant Quality Score Recalibration (VQSR) was conducted based on HapMap 3.3, NCBI Variation Database (dbSNP138), 1,000 Genomes and Omni 2.5M SNP chip array. The variants' functional information was annotated using SnpEff 4.2 (GRCh 37.75; ref. 54).

Immunoprecipitation Assays

For immunoprecipitation, we used protein G beads. Following gel electrophoresis, proteins were transferred onto a nitrocellulose membrane. The membrane was blocked in TBST buffer (pH 7.5; 0.02 M tris-HCl, 0.15 M NaCl, and 0.05% Tween 20) containing albumin (3%), blotted with a primary antibody (overnight at cold), washed in TBST, and incubated for 30 minutes with a secondary antibody conjugated to horseradish peroxidase.

BLISS and Comet Assays

BLISS was performed as previously described (55). For comet assays, cells (2.5×10^5) were treated with drugs, and 24 hours later we used the alkaline electrophoresis buffer and a kit from Abcam. Comets stained with FITC were viewed using an Olympus XM10 epifluorescence microscope and analyzed using the CASPlab software.

Digital PCR

Mutation analysis specific for the T790M alteration was performed using the Bio-Rad droplet digital PCR (ddPCR) platform. PC9ER cells, which harbor the T790M mutation, were used as positive

control. Cycling conditions were as follows: 95°C for 10 minutes (1 cycle), 40 cycles at 94°C for 30 seconds, and 55°C for 1 minute, followed by 98°C for 10 minutes and hold at 4°C. The count of partitions showing positive amplification was obtained using the QuantaSoft Software.

RPPA Profiling

Lysates were adjusted to a total protein concentration of 2 μg/μL, mixed with 4 × SDS sample buffer and denatured at 95°C. Lysates and dilution series of each cell line were spotted as technical triplicates on nitrocellulose-coated glass slides (Grace-Biolabs). Post spotting, slides were incubated with the blocking buffer containing 5 mmol/L NaF and 1 mmol/L Na_3VO_4, prior to overnight incubation with primary antibodies at 4°C. Primary antibodies were detected using Alexa Fluor 680–coupled goat anti-mouse IgG (Life Technologies). In addition, representative slides were stained for total protein quantification using Fast Green FCF protein dye. Signal intensities were quantified using GenePixPro 7.0 (Molecular Service). Data preprocessing, merging of technical triplicates, and background correction were performed using the RPPanalyzer Rpackage.

ROS Production Assay

Cells were seeded on 96-well white-walled plates (10^4 cells/well) and incubated overnight for attachment. The following day, cells were treated as indicated, and after 48 hours ROS were measured using the ROS-Glo H_2O_2 kit (Promega). Luminescence was measured using a plate-reading luminometer (TECAN, Infinite 200 PRO Nano Quant) and the resulting data were normalized to untreated cells at each time point.

PLA

Cells plated on glass coverslips were fixed, permeabilized, blocked, and incubated with the indicated antibodies. PLA was performed using the DuoLink In Situ PLA Detection Kit (Sigma). Hybridization with PLA probes, ligation, and amplification of the signal were performed according to the manufacturer's instructions. Images were taken using Zeiss LSM800 confocal microscope. PLA signals were quantified per cell using the ImageJ software. Experiments were performed in triplicates, and 20 cells were used per condition.

Metabolite Extraction and LC/MS Polar Metabolite Analysis

Polar substance extraction and analysis were performed as previously described (56) with some modifications: cell extracts were mixed with a precooled (−20°C) homogeneous methanol:methyl-tertbutyl-ether (TMBE), 1:3 (v/v) mixture. The tubes were sonicated for 30 minutes in an ice-cold sonication bath. Then, UPLC grade water:methanol (3:1, v/v) solution (0.5 mL) containing internal standards (a mixture of 13C- and 15N-labeled amino acids, from Sigma) was added to the tubes, followed by centrifugation. Then, the polar phase was reextracted. Finally, samples were lyophilized and the pellets were dissolved using 0.15 mL water:methanol (1:1), and centrifuged twice prior to loading onto the LC/MS system. Metabolic profiling was performed using Acquity I class UPLC System combined with a mass spectrometer (Thermo Exactive Plus Orbitrap). LC separation was performed using a SeQuant Zic-pHilic column with the SeQuant guard column. The mobile phases used were 20 mmol/L ammonium carbonate with 0.1% ammonium hydroxide in water:acetonitrile (80:20, v/v; mobile phase A) and acetonitrile as mobile phase B. The flow rate was kept at 0.2 mL per minute and the following gradient: 0–2 minutes 75% of B, 14 minutes 25% of B, 18 minutes 25% of B, 19 minutes 75% of B, for 4 minutes. For data processing, we used TraceFinder (Thermo Fisher).

Colony Formation and Thymidine Incorporation Assays

Cells were sparsely seeded in 6-well plates and later treated for 21 days with drugs. Colonies were fixed in 4% paraformaldehyde and stained with crystal violet. Finally, the plates were inspected using microscopy and the numbers of colonies were determined. For thymidine incorporation assays, cells were plated onto 24-well plates at a density of 5×10^4 cells/well. Sixteen hours later, cells were incubated with a fresh serum-free medium containing ^{3}H-thymidine (1 μCi). After 48 hours, the reaction was terminated by the addition of ice-cold trichloroacetic acid (5%). Quadruplicate samples were collected into scintillation vials.

Luciferase Reporter Assays

Cells were cotransfected with a luciferase reporter plasmid, along with pGL3-Control (Promega). Luciferase activity was determined using the dual-luciferase reporter assay system (Promega). Firefly luciferase luminescence values were normalized to Renilla luminescence.

Nucleotide Sequencing of RNA and Differential Expression Analysis

RNA-seq libraries were prepared as follows: polyA fractions (mRNA) were purified from 500 ng of total input RNA followed by fragmentation and the generation of double-stranded cDNA. Later, we performed Agencourt Ampure XP beads cleanup (Beckman Coulter), end repair, A base addition, adapter ligation, and PCR amplification. Libraries were quantified using Qubit (Thermo Fisher Scientific) and TapeStation (Agilent). Sequencing was done on a HiSeq instrument (Illumina) using a 60-cycle kit, allocating ~250 M reads total (single read sequencing). Genes were considered differentially expressed if their P value was smaller than or equal to 5e−06, and the log fold-change threshold was ±1. The tool "Enrichr" was used to perform pathway enrichment analysis.

Immunofluorescence, Cell Viability, and Cell-Cycle Analyses

These assays were performed as we previously described (15).

Animal Experiments

All animal studies were approved by the Weizmann Institute's board and they were performed in accordance with the guidelines of the Institutional Animal Care and Use Committee. PC9 cells (2.5×10^6 per mouse, in 0.1 mL) were subcutaneously injected into the right flanks of CD1 nude mice (5–6 weeks old). Once tumors reached volumes of approximatively 500 mm^3, mice were randomized and treated as indicated. TKIs were administered daily using oral gavage. Antibodies were administered twice a week using intraperitoneal injections. Tumor volume was estimated using vernier caliper measurements. Animals were euthanized when tumor size reached 1,400–1,500 mm^3. For metastasis assays, NOG mice were injected intravenously (2×10^5 cells per mouse). Mice were sacrificed four weeks after injection, and the lungs were analyzed.

Human Subjects, Analyses of Clinical Data, and Thin Tumor Sections

We obtained from all relevant patients written informed consent for analyses of clinical correlates and tissue collection. The studies were conducted in accordance with the Declaration of Helsinki, the Belmont Report, and the U.S. Common Rule. The studies were approved by institutional review boards at the University of California (San Francisco) and at the University of Bologna (Italy). Archival formalin-fixed paraffin-embedded tumor blocks were cut at 4-μm thickness, deparaffinized, and then rehydrated. Bleaching was performed in 3% hydrogen peroxide and epitopes were retrieved using either citrate

buffer (pH 6.1) or the universal retrieval buffer. Following blocking, sections were incubated overnight with the primary antibody, and on the next day slides were rinsed and incubated with the respective secondary antibody. Images were captured using a Leica confocal imager or they were digitized using an Aperio AT2 Slide Scanner. Immunoreactivity was evaluated using ImageJ or Aperio ScanScope software. Staining intensity was returned using the following scale: 0 (0%–10% of tissue stained positive), 1 (10%–30%), 2 (30%–70%), and 3 (>70%). Scores were generated from five different slide areas.

Statistical Analyses

Microsoft Excel, GraphPad Prism (version 8.0.2), and the R (version 3.6.2) software packages were used to analyze the data. Statistical analyses were performed using Fisher exact test and one- or two-way ANOVA with the Dunnett or Tukey test (*, $P \leq 0.05$; **, $P \leq 0.01$; ***, $P \leq 0.001$; ****, $P \leq 0.0001$). Flow cytometry analysis was performed on a BD FACSAria Fusion Instrument. Further analysis was performed using the FlowJo software v10.2 (Tree Star). Staining intensity was determined using ImageJ.

Data and Materials Availability

The RNA-seq data sets generated in this study are available at the Gene Expression Omnibus under accession number GSE202342. All data and materials will be made available to any researcher for purposes of reproducing or extending the analyses. Requests for reagents should be addressed to Y. Yarden.

Authors' Disclosures

A. Noronha reports a patent application (pending) dealing with drug combinations aimed at preventing drug resistance. A. Ardizzoni reports personal fees from AstraZeneca, Roche, Bristol Myers Squibb, MSD, Sanofi, Takeda, Eli Lilly, and Bayer outside the submitted work. M. Oren reports that his daughter Y. Oren is also a coauthor but that her collaborative contribution to the study (at the Broad Institute) was totally separate from his collaborative contribution (at the Weizmann Institute). C.M. Blakely reports grants from AstraZeneca, Novartis, Takeda, Mirati, and Spectrum, and personal fees from Janssen, Oncocyte, Amgen, Blueprint Medicines, and Bayer outside the submitted work. A. Regev reports personal fees and other support from Celsius Therapeutics, Immunitas, and Syros, personal fees from Thermo Fisher Scientific, and other support from Genentech/Roche and Neogene Therapeutics during the conduct of the study, as well as various patents in single-cell genomics licensed to Celsius Therapeutics and Immunitas. G. Getz reports grants from IBM during the conduct of the study; grants from Pharmacyclics outside the submitted work; is an inventor on patent applications related to MSMuTect, MSMutSig, MSIDetect, POLYSOLVER, and SignatureAnalyzer-GPU; and is a founder of and consultant for and has privately held equity in Scorpion Therapeutics. Y. Yarden reports grants from the Israel Science Foundation, the European Research Council, and the Adelson Medical Research Foundation during the conduct of the study, as well as patent application submitted by Yeda (pending) dealing with drug combinations aimed at preventing drug resistance. No disclosures were reported by the other authors.

Authors' Contributions

A. Noronha: Conceptualization, formal analysis, investigation, methodology. **N. Belugali Nataraj:** Validation, investigation. **J. Sang Lee:** Data curation. **B. Zhitomirsky:** Data curation, investigation. **Y. Oren:** Data curation. **S. Oster:** Formal analysis, investigation, methodology. **M. Lindzen:** Formal analysis, investigation. **S. Mukherjee:** Formal analysis, methodology. **R. Will:** Formal analysis, methodology. **S. Ghosh:** Formal analysis, methodology. **A. Simoni-Nieves:** Methodology. **A. Verma:** Methodology. **R. Chatterjee:** Methodology. **S. Borgoni:** Data curation, formal analysis, methodology. **W. Robinson:** Data curation. **S. Sinha:** Formal analysis. **A. Brandis:** Data curation, formal analysis, methodology. **D.L. Kerr:** Formal analysis, methodology. **W. Wu:** Data curation. **A. Sekar:** Methodology. **S. Giri:** Methodology. **Y. Chung:** Data curation. **D. Drago-Garcia:** Formal analysis. **B.P. Danysh:** Formal analysis, methodology. **M. Lauriola:** Formal analysis, methodology. **M. Fiorentino:** Formal analysis, methodology. **A. Ardizzoni:** Investigation. **M. Oren:** Investigation. **C.M. Blakely:** Formal analysis, supervision, methodology. **J. Ezike:** Data curation. **S. Wiemann:** Investigation. **L. Parida:** Investigation. **T.G. Bivona:** Supervision. **R.I. Aqeilan:** Supervision. **J.S. Brugge:** Supervision. **A. Regev:** Supervision. **G. Getz:** Supervision. **E. Ruppin:** Supervision. **Y. Yarden:** Conceptualization, supervision, writing–original draft, writing–review and editing.

Acknowledgments

We thank Tomer Meir Salame, Tevi Mehlman, Orit Leitner, Hedva Hamawi, Gilgi Friedlander, and Roni Oren for methodologic help and advice and Moshe Elkabets for reagents. This work was performed in the Marvin Tanner Laboratory for Research on Cancer. Y. Yarden is the incumbent of the Harold and Zelda Goldenberg Professorial Chair in Molecular Cell Biology. Our studies are supported by the Israel Science Foundation (ISF; 1931/20), the European Research Council (ERC; 740469), and the Dr. Miriam and Sheldon G. Adelson Medical Research Foundation (AMRF; to M. Oren, J.S. Brugge, G. Getz, and Y. Yarden). Funding for sequencing and fellowships of B. Zhitomirsky and B.P. Danysh was provided by the Broad/IBM Cancer Resistance Research Project (given to G. Getz and L. Parida). Y. Oren was supported by the Hope Fund for Cancer Research, Grillo-Marxuach Postdoctoral Fellowship, and the Rivkin Scientific Scholar Award.

The publication costs of this article were defrayed in part by the payment of publication fees. Therefore, and solely to indicate this fact, this article is hereby marked "advertisement" in accordance with 18 USC section 1734.

Note

Supplementary data for this article are available at Cancer Discovery Online (http://cancerdiscovery.aacrjournals.org/).

Received January 28, 2022; revised May 10, 2022; accepted July 25, 2022; published first July 27, 2022.

REFERENCES

1. Radman M. SOS repair hypothesis: phenomenology of an inducible DNA repair which is accompanied by mutagenesis. Basic Life Sci 1975;5A:355–67.
2. Al Mamun AA, Lombardo MJ, Shee C, Lisewski AM, Gonzalez C, Lin D, et al. Identity and function of a large gene network underlying mutagenic repair of DNA breaks. Science 2012;338:1344–8.
3. Baharoglu Z, Mazel D. SOS, the formidable strategy of bacteria against aggressions. FEMS Microbiol Rev 2014;38:1126–45.
4. Fitzgerald DM, Hastings PJ, Rosenberg SM. Stress-induced mutagenesis: implications in cancer and drug resistance. Annu Rev Cancer Biol 2017;1:119–40.
5. Russo M, Crisafulli G, Sogari A, Reilly NM, Arena S, Lamba S, et al. Adaptive mutability of colorectal cancers in response to targeted therapies. Science 2019;366:1473–80.
6. Cipponi A, Goode DL, Bedo J, McCabe MJ, Pajic M, Croucher DR, et al. MTOR signaling orchestrates stress-induced mutagenesis, facilitating adaptive evolution in cancer. Science 2020;368:1127–31.
7. Garraway LA, Janne PA. Circumventing cancer drug resistance in the era of personalized medicine. Cancer Discov 2012;2:214–26.
8. Konieczkowski DJ, Johannessen CM, Garraway LA. A convergence-based framework for cancer drug resistance. Cancer Cell 2018;33:801–15.

9. Sharma SV, Lee DY, Li B, Quinlan MP, Takahashi F, Maheswaran S, et al. A chromatin-mediated reversible drug-tolerant state in cancer cell subpopulations. Cell 2010;141:69–80.
10. Pao W, Miller VA, Politi KA, Riely GJ, Somwar R, Zakowski MF, et al. Acquired resistance of lung adenocarcinomas to gefitinib or erlotinib is associated with a second mutation in the EGFR kinase domain. PLoS Med 2005;2:e73.
11. Kobayashi S, Boggon TJ, Dayaram T, Janne PA, Kocher O, Meyerson M, et al. EGFR mutation and resistance of non-small-cell lung cancer to gefitinib. N Engl J Med 2005;352:786–92.
12. Oxnard GR, Arcila ME, Chmielecki J, Ladanyi M, Miller VA, Pao W. New strategies in overcoming acquired resistance to epidermal growth factor receptor tyrosine kinase inhibitors in lung cancer. Clin Cancer Res 2011;17:5530–7.
13. Engelman JA, Zejnullahu K, Mitsudomi T, Song Y, Hyland C, Park JO, et al. MET amplification leads to gefitinib resistance in lung cancer by activating ERBB3 signaling. Science 2007;316:1039–43.
14. Mancini M, Gal H, Gaborit N, Mazzeo L, Romaniello D, Salame TM, et al. An oligoclonal antibody durably overcomes resistance of lung cancer to third-generation EGFR inhibitors. EMBO Mol Med 2018;10:294–308.
15. Romaniello D, Mazzeo L, Mancini M, Marrocco I, Noronha A, Kreitman M, et al. A combination of approved antibodies overcomes resistance of lung cancer to osimertinib by blocking bypass pathways. Clin Cancer Res 2018;24:5610–21.
16. Taniguchi H, Yamada T, Wang R, Tanimura K, Adachi Y, Nishiyama A, et al. AXL confers intrinsic resistance to osimertinib and advances the emergence of tolerant cells. Nat Commun 2019;10:259.
17. Zhang Z, Lee JC, Lin L, Olivas V, Au V, LaFramboise T, et al. Activation of the AXL kinase causes resistance to EGFR-targeted therapy in lung cancer. Nat Genet 2012;44:852–60.
18. Engelman JA, Janne PA. Mechanisms of acquired resistance to epidermal growth factor receptor tyrosine kinase inhibitors in non-small cell lung cancer. Clin Cancer Res 2008;14:2895–9.
19. Haga Y, Marrocco I, Noronha A, Uribe ML, Nataraj NB, Sekar A, et al. Host-dependent phenotypic resistance to EGFR tyrosine kinase inhibitors. Cancer Res 2021;81:3862–75.
20. Graham DK, DeRyckere D, Davies KD, Earp HS. The TAM family: phosphatidylserine sensing receptor tyrosine kinases gone awry in cancer. Nat Rev Cancer 2014;14:769–85.
21. Salgia R, Kulkarni P. The genetic/non-genetic duality of drug 'resistance' in cancer. Trends Cancer 2018;4:110–8.
22. Kimura H, Suminoe M, Kasahara K, Sone T, Araya T, Tamori S, et al. Evaluation of epidermal growth factor receptor mutation status in serum DNA as a predictor of response to gefitinib (IRESSA). Br J Cancer 2007;97:778–84.
23. Oren Y, Tsabar M, Cuoco MS, Amir-Zilberstein L, Cabanos HF, Hutter JC, et al. Cycling cancer persister cells arise from lineages with distinct programs. Nature 2021;596:576–82.
24. Roper N, Brown AL, Wei JS, Pack S, Trindade C, Kim C, et al. Clonal evolution and heterogeneity of osimertinib acquired resistance mechanisms in EGFR mutant lung cancer. Cell Rep Med 2020;1:1100007.
25. Yan WX, Mirzazadeh R, Garnerone S, Scott D, Schneider MW, Kallas T, et al. BLISS is a versatile and quantitative method for genome-wide profiling of DNA double-strand breaks. Nat Commun 2017; 8:15058.
26. Pierce AJ, Johnson RD, Thompson LH, Jasin M. XRCC3 promotes homology-directed repair of DNA damage in mammalian cells. Genes Dev 1999;13:2633–8.
27. Yang W, Gao Y. Translesion and repair DNA polymerases: diverse structure and mechanism. Annu Rev Biochem 2018;87:239–61.
28. Yang Y, Gao Y, Zlatanou A, Tateishi S, Yurchenko V, Rogozin IB, et al. Diverse roles of RAD18 and Y-family DNA polymerases in tumorigenesis. Cell Cycle 2018;17:833–43.
29. Maynard A, McCoach CE, Rotow JK, Harris L, Haderk F, Kerr DL, et al. Therapy-induced evolution of human lung cancer revealed by single-cell RNA sequencing. Cell 2020;182:1232–51.
30. Stelter P, Ulrich HD. Control of spontaneous and damage-induced mutagenesis by SUMO and ubiquitin conjugation. Nature 2003;425: 188–91.
31. Bienko M, Green CM, Crosetto N, Rudolf F, Zapart G, Coull B, et al. Ubiquitin-binding domains in Y-family polymerases regulate translesion synthesis. Science 2005;310:1821–4.
32. Gao Y, Mutter-Rottmayer E, Greenwalt AM, Goldfarb D, Yan F, Yang Y, et al. A neomorphic cancer cell-specific role of MAGE-A4 in trans-lesion synthesis. Nat Commun 2016;7:12105.
33. Guan J, Zheng X. NEDDylation regulates RAD18 ubiquitination and localization in response to oxidative DNA damage. Bichem Biophys Res Commun 2018;508:1240–4.
34. Hata AN, Niederst MJ, Archibald HL, Gomez-Caraballo M, Siddiqui FM, Mulvey HE, et al. Tumor cells can follow distinct evolutionary paths to become resistant to epidermal growth factor receptor inhibition. Nat Med 2016;22:262–9.
35. Schmidt TT, Reyes G, Gries K, Ceylan CU, Sharma S, Meurer M, et al. Alterations in cellular metabolism triggered by URA7 or GLN3 inactivation cause imbalanced dNTP pools and increased mutagenesis. Proc Natl Acad Sci U S A 2017;114:E4442–E51.
36. Huang M, Elledge SJ. Identification of RNR4, encoding a second essential small subunit of ribonucleotide reductase in Saccharomyces cerevisiae. Mol Cell Biol 1997;17:6105–13.
37. Bester AC, Roniger M, Oren YS, Im MM, Sarni D, Chaoat M, et al. Nucleotide deficiency promotes genomic instability in early stages of cancer development. Cell 2011;145:435–46.
38. Lee JS, Adler L, Karathia H, Carmel N, Rabinovich S, Auslander N, et al. Urea cycle dysregulation generates clinically relevant genomic and biochemical signatures. Cell 2018;174:1559–70.
39. Ben-Sahra I, Hoxhaj G, Ricoult SJH, Asara JM, Manning BD. mTORC1 induces purine synthesis through control of the mitochondrial tetrahydrofolate cycle. Science 2016;351:728–33.
40. Hong J, Maacha S, Belkhiri A. Transcriptional upregulation of c-MYC by AXL confers epirubicin resistance in esophageal adenocarcinoma. Mol Oncol 2018;12:2191–208.
41. Keshet R, Lee JS, Adler L, Iraqi M, Ariav Y, Lim LQJ, et al. Targeting purine synthesis in ASS1-expressing tumors enhances the response to immune checkpoint inhibitors. Nature Cancer 2020;1:894–908.
42. Kortlever RM, Sodir NM, Wilson CH, Burkhart DL, Pellegrinet L, Brown Swigart L, et al. Myc cooperates with ras by programming inflammation and immune suppression. Cell 2017;171:1301–15.
43. Chandriani S, Frengen E, Cowling VH, Pendergrass SA, Perou CM, Whitfield ML, et al. A core MYC gene expression signature is prominent in basal-like breast cancer but only partially overlaps the core serum response. PLoS One 2009;4:e6693.
44. Ishikawa M, Sonobe M, Nakayama E, Kobayashi M, Kikuchi R, Kitamura J, et al. Higher expression of receptor tyrosine kinase Axl, and differential expression of its ligand, Gas6, predict poor survival in lung adenocarcinoma patients. Ann Surg Oncol 2013;20 Suppl 3:S467–76.
45. Pirazzoli V, Ayeni D, Meador CB, Sanganahalli BG, Hyder F, de Stanchina E, et al. Afatinib plus cetuximab delays resistance compared to single-agent erlotinib or afatinib in mouse models of TKI-Naive EGFR L858R-induced lung adenocarcinoma. Clin Cancer Res 2016;22:426–35.
46. Pribis JP, Garcia-Villada L, Zhai Y, Lewin-Epstein O, Wang AZ, Liu J, et al. Gamblers: an antibiotic-induced evolvable cell subpopulation differentiated by reactive-oxygen-induced general stress response. Mol Cell 2019;74:785–800.
47. Stine ZE, Walton ZE, Altman BJ, Hsieh AL, Dang CV. MYC, metabolism, and cancer. Cancer Discov 2015;5:1024–39.
48. Mathews CK. DNA precursor metabolism and genomic stability. FASEB J 2006;20:1300–14.
49. Nishimura T, Nakata A, Chen X, Nishi K, Meguro-Horike M, Sasaki S, et al. Cancer stem-like properties and gefitinib resistance are dependent on purine synthetic metabolism mediated by the mitochondrial enzyme MTHFD2. Oncogene 2019;38:2464–81.
50. Muller J, Krijgsman O, Tsoi J, Robert L, Hugo W, Song C, et al. Low MITF/AXL ratio predicts early resistance to multiple targeted drugs in melanoma. Nat Commun 2014;5:5712.
51. Badarni M, Prasad M, Balaban N, Zorea J, Yegodayev KM, Joshua BZ, et al. Repression of AXL expression by AP-1/JNK blockage overcomes resistance to PI3Ka therapy. JCI Insight 2019;5:e125341.

52. Turke AB, Zejnullahu K, Wu Y-L, Song Y, Dias-Santagata D, Lifshits E, et al. Preexistence and clonal selection of MET amplification in EGFR mutant NSCLC. Cancer Cell 2010;17:77–88.
53. Wang R, Yamada T, Kita K, Taniguchi H, Arai S, Fukuda K, et al. Transient IGF-1R inhibition combined with osimertinib eradicates AXL-low expressing EGFR mutated lung cancer. Nat Commun 2020;11:4607.
54. Cingolani P, Platts A, Wang le L, Coon M, Nguyen T, Wang L, et al. A program for annotating and predicting the effects of single nucleotide polymorphisms, SnpEff: SNPs in the genome of Drosophila melanogaster strain w1118; iso-2; iso-3. Fly (Austin) 2012;6:80–92.
55. Hazan I, Monin J, Bouwman BAM, Crosetto N, Aqeilan RI. Activation of oncogenic super-enhancers is coupled with DNA repair by RAD51. Cell Rep 2019;29:560–72.
56. Malitsky S, Ziv C, Rosenwasser S, Zheng S, Schatz D, Porat Z, et al. Viral infection of the marine alga Emiliania huxleyi triggers lipidome remodeling and induces the production of highly saturated triacylglycerol. New Phytol 2016;210:88–96.